

Published in final edited form as:

*Neuron*. 2009 July 30; 63(2): 171–177. doi:10.1016/j.neuron.2009.06.023.

## Synapse Distribution Suggests a Two-Stage Model of Dendritic Integration in CA1 Pyramidal Neurons

Yael Katz<sup>1,2</sup>, Vilas Menon<sup>3</sup>, Daniel A. Nicholson<sup>1,5</sup>, Yuri Geinisman<sup>5</sup>, William L. Kath<sup>1,3,4</sup>, and Nelson Spruston<sup>1,\*</sup>

<sup>1</sup>Department of Neurobiology and Physiology, Northwestern University, Evanston, IL 60208, USA

<sup>2</sup>Interdepartmental Biological Sciences Program, Northwestern University, Evanston, IL 60208, USA

<sup>3</sup>Department of Engineering Sciences and Applied Mathematics, Northwestern University, Evanston, IL 60208, USA

<sup>4</sup>Northwestern Institute on Complex Systems, Northwestern University, Evanston, IL 60208, USA

<sup>5</sup>Department of Cell and Molecular Biology, Northwestern University Feinberg School of Medicine, Chicago, IL 60611, USA

### SUMMARY

Competing models have been proposed to explain how neurons integrate the thousands of inputs distributed throughout their dendritic trees. In a simple global integration model, inputs from all locations sum in the axon. In a two-stage integration model, inputs contribute directly to dendritic spikes, and outputs from multiple branches sum in the axon. These two models yield opposite predictions of how synapses at different dendritic locations should be scaled if they are to contribute equally to neuronal output. We used serial-section electron microscopy to reconstruct individual apical oblique dendritic branches of CA1 pyramidal neurons and observe a synapse distribution consistent with the two-stage integration model. Computational modeling suggests that the observed synapse distribution enhances the contribution of each dendritic branch to neuronal output.

### INTRODUCTION

Pyramidal neurons have extended apical and basal dendritic trees, covered with synapses that collect inputs from their network partners. Understanding how these inputs are integrated into all-or-none action-potential output is fundamental to understanding how circuits function in the cerebral cortex. As other work progresses toward understanding the electrophysiological and behavioral implications of different synaptic inputs (Brun et al., 2008; Brun et al., 2002) as well as the molecular basis of the function and plasticity of individual synapses (Harvey and Svoboda, 2007; Harvey et al., 2008; Tanaka et al., 2008), it is equally important to understand how these inputs are integrated at the cellular level and

© 2009 Elsevier Inc. All rights reserved

\*Correspondence: spruston@northwestern.edu.

**Publisher's Disclaimer:** This is a PDF file of an unedited manuscript that has been accepted for publication. As a service to our customers we are providing this early version of the manuscript. The manuscript will undergo copyediting, typesetting, and review of the resulting proof before it is published in its final citable form. Please note that during the production process errors may be discovered which could affect the content, and all legal disclaimers that apply to the journal pertain.

**SUPPLEMENTAL DATA** The Supplemental Data include two figures and six movies.

how this integration is shaped by plasticity (Losonczy et al., 2008). Because pyramidal neurons often span millimeter distances and have tens of millimeters of branching dendritic cable (Amaral and Witter, 1989), a crucial question is whether all inputs contribute equally to neuronal output or are weighted by their locations (Häusser, 2001).

Pyramidal neurons can operate in two integration modes (Gasparini and Magee, 2006). In the global integration mode, inputs contribute directly to neuronal output by triggering excitatory postsynaptic potentials (EPSPs) that propagate to the action potential initiation zone in the axon. The axon integrates the contribution from each input, and if the resulting voltage is above threshold, an action potential is generated. In the two-stage integration mode, inputs activate voltage-gated channels in the dendrites and trigger dendritic spikes (Gasparini et al., 2004; Golding and Spruston, 1998). Output from each branch, rather than each synapse, then propagates forward to the axon where a global summation takes place (Gasparini and Magee, 2006; Polsky et al., 2004).

Cable theory predicts that the contributions of inputs to the somatic and dendritic membrane potentials will depend on their locations (Rall, 1959; Spruston, 2008). Inputs that arrive close to the soma will have a larger influence on axonal action potential output than more distal inputs, which attenuate more by the time they reach the action potential initiation zone (Golding et al., 2005; Rall, 1959). Distal inputs, however, lead to larger local dendritic voltage changes compared to their more proximal counterparts, due to differences in input resistance along individual dendritic branches. Small-diameter dendritic segments near branch ends tend to have the highest input resistance, which decreases towards the branch origin where the conductance due to larger dendritic branches and the soma is greatest. Thus, proximal inputs will have relatively large effects in the soma but smaller effects in the dendrite, and distal inputs will have relatively small effects in the soma but larger local effects in the dendrite.

Despite the fact that this prediction follows from basic principles of cable theory that have been well understood for at least fifty years, how pyramidal neurons balance these competing effects has never been directly tested. Experiments in CA1 pyramidal neurons show that for limited distances along the somato-dendritic axis, neurons normalize the representation of inputs at the soma by increasing synaptic strength to balance attenuation of synaptic current (Magee and Cook, 2000; Nicholson et al., 2006). Whether synaptic conductance is scaled in this manner along individual dendritic branches, however, is not known.

This is a critical issue because if inputs are to contribute approximately equally to neuronal output, then the global and two-stage integration modes suggest opposite distributions of synaptic strength along individual dendritic branches. If neurons are optimized for the global integration mode, synapses farthest from the soma should have the largest conductance in order to compensate for charge attenuation, so synaptic conductance should increase from the origin to the end of individual dendritic branches (Figure 1A, left). If neurons instead are optimized for the two-stage integration mode, synapses farthest from the soma should be the weakest, in order to balance the high input impedance near branch ends, and thus synaptic conductance should decrease from the origin to the end of individual dendritic branches (Figure 1A, right).

To ascertain what synapse distribution is actually present in CA1 pyramidal neurons, we used serial-section electron microscopy (ssEM) to reconstruct excitatory synapses along individually labeled apical oblique dendrites. This approach differs from previous ssEM experiments (Megias et al., 2001; Nicholson and Geinisman, 2009; Nicholson et al., 2006), which involved sectioning blocks of tissue to obtain measurements that are an average over

many neurons and dendritic locations. By determining the synapse distribution along individual dendrites, we could infer whether the synapse distribution in CA1 pyramidal neurons favors a global or two-stage integration mode.

## RESULTS AND DISCUSSION

We injected biotinylated dextran amine (BDA) into the rat hippocampus in vivo to achieve sparse labeling of CA1 neurons (see Experimental Procedures). We then used light microscopy to select isolated neurons with clearly labeled spiny dendrites. Using ssEM (Figure 1B,C,D; S1), we reconstructed three apical oblique dendrites in their entirety, and for each branch we made within-dendrite comparisons of the synapses near the branch origin, center of the branch, and those near the branch end (Figure 1E, bottom). Additionally, we reconstructed three proximal and two distal dendritic segments from different branches, identified by the branch point with the primary apical dendrite and the termination of the dendritic branch, respectively (Figure 1E, top), and performed between-dendrite comparisons of these segments. Analysis was restricted to dendritic segments at least 10  $\mu\text{m}$  long and spines that were completely contained within the serial sections. A total of over 3,000 sections were analyzed. In all cases, spines were completely filled and traceable to their parent dendrite and in many cases post-synaptic densities (PSDs) were clearly visible (spine  $n = 433$  proximal and  $n = 189$  distal; PSD  $n = 195$  proximal and  $n = 78$  distal; Figures 1B,C,D; S1). Spine volume and PSD area measurements were within the range reported in other studies (Harris et al., 1992; Harris and Stevens, 1989; Nicholson and Geinisman, 2009; Nicholson et al., 2006).

We found two major differences between spines on dendritic segments near branch origins and those near branch ends. First, spine density was approximately 50% greater in near-branch-origin segments compared to those near branch ends (t-test,  $p < 0.003$ ) (Figure 1F). Second, the distribution of spine volumes was skewed toward larger spines in dendritic segments near branch origins ( $\chi^2 = 20.4$ ;  $p < 0.05$ ; Figure 1G).

We also compared synapses near branch origins to those near branch ends. Though we found a variety of synapse shapes and sizes at all dendritic locations (Figure 2A), the distribution of PSD areas was heavily skewed toward larger PSDs near branch origins ( $\chi^2 = 354.9$ ;  $p < 0.00001$ ; Figure 2B). This trend was present in the overall analysis (Figure 2B; mean PSD area  $0.057 \mu\text{m}^2$  near branch origins and  $0.030 \mu\text{m}^2$  near branch ends), as well in each within-dendrite comparison (Figure S2).

To control for the possibility that synapses near the terminal portion of the dendrite are unusual, we also analyzed 101 spines and synapses in three dendritic segments from the middle of the branch. We found that in each of these segments spine density and the distributions of spine volume and PSD area were more similar to the distributions near the dendrite's terminal end than near its origin (Figures 1E–G, 2B, and S2), suggesting that the decline in these values is not restricted to the most terminal portion of dendritic branches. Spine volume near the center of the branch appeared to be smaller than near branch ends; the significance of this result will require further study.

To quantify the relationship between spine volume or PSD area and synaptic strength (Kharazia et al., 1996; Kharazia and Weinberg, 1999), we performed immunogold labeling of AMPA receptors (Figures 2C,D). We analyzed synapses and their parent spines ( $n = 342$ ) from area CA1 stratum radiatum of the hippocampus, each of which could be traced back to their spine necks. We found both spine volume and PSD area were strongly correlated with the number of gold particles (Figure 2E,  $R^2 = 0.7216$ ,  $p < 0.001$ ; Figure 2F,  $R^2 = 0.7567$ ,  $p < 0.001$ ), indicating that these measures provide reasonable estimates of relative synaptic strength. Thus, assuming that PSDs on different dendritic segments have similar receptor

properties, the approximately two-fold reduction in PSD size at the branch end relative to the branch origin suggests that near-branch-end synapses are about half as strong as their near-branch-origin counterparts. From these data we conclude that synapse strength is scaled within each dendrite to reduce the impact of location-dependent differences in dendritic depolarization due to varying input impedance along the branch.

To investigate the functional implications of the synapse distribution that we observed, we incorporated our experimental findings into a computational model. Using a reconstructed CA1 pyramidal neuron morphology with excitable dendrites (see Experimental Procedures; Figure 3A), we distributed synapses along each apical oblique branch according to the experimentally determined gradient, with synapse density and strength both decreasing from branch origin to branch end in a step-like manner after the first third of the branch. Groups of synapses throughout each branch were randomly selected (from the actual distribution of PSD areas; see Experimental Procedures) and activated, often leading to the initiation of dendritic spikes (60–80 mV amplitude; Figure 3B). Spikes tended to initiate near the end of each branch, attenuating severely by the time they reached the primary apical dendrite and even further between this location and the soma, consistent with experimental data (Losonczy and Magee, 2006). The number of activated synapses required to trigger a dendritic spike varied because synapse locations and hence strengths were chosen randomly, so simulations were repeated to determine average responses to activation of different populations of synapses on the same branch (500 trials for each branch). The average number of activated synapses needed for a dendritic spike varied between branches as well, but across all branches an average of approximately 10 synapses triggered a dendritic spike, again consistent with experimental data (Losonczy and Magee, 2006).

We performed a comparison between this experimentally based model and the hypothetical model predicted if synapses were instead distributed to normalize the contribution of inputs to global integration in the axon. In this hypothetical “global integration model” synapse density was uniform and synaptic conductance was chosen to approximately normalize the somatic depolarization produced by inputs along each apical branch (keeping the total synaptic conductance the same as in the experimentally-based model). We then repeated the same simulations. If synaptic conductance is indeed scaled to normalize the contribution of inputs to dendritic spike initiation, we would expect the location of the last input selected – the one that brings the branch above spike threshold – to be uniformly distributed (Figure 3C, dashed line). In the global integration model, inputs near branch ends were approximately 9.4 times more likely to trigger a dendritic spike as inputs near branch origins (Figure 3C, black). In our experimentally-based model, inputs near branch ends were only 2.7 times as likely to bring the branch above dendritic-spike threshold as those near branch origins (Figure 3C, blue). Because of the high input resistance associated with branch ends, this means that dendritic spikes are often triggered by small numbers of inputs near branch ends in the global integration model, a situation greatly reduced in the model based on the actual synapse distribution. Thus, the experimentally observed distribution helps to normalize the likelihood for synapses at different positions to contribute to a dendritic spike.

A second important consequence of the synapse distribution we observed is that it increases the contribution of a dendritic branch to axonal action potentials (Figure 3D; Movie S1–6). Despite the fact that dendritic spikes occurred more frequently in the model predicted by global synaptic integration, when fixed numbers of synapses on a branch were activated in the two models, the depolarization measured at the soma tended to be greater in the model based on the actual synapse distribution (Figure 3D,E). The global integration model only produced a larger response when a small number of synapses were activated, leading to a much higher likelihood of dendritic spike initiation owing to the prevalence of strong synapses on the high-impedance terminal portions of the branch (Figure 3D). The enhanced

representation of each branch at the soma in the two-stage integration model was attributable primarily to the larger numbers of stronger synapses close to the branch origin. By contrast, in the global integration model (or even with a uniform distribution of synaptic density and strength; not shown), synaptic weight is shifted more distally and thus the output of each branch is reduced.

Our model predicts that the ability of individual dendritic branches to influence axonal output should decrease with the distance of the branch origin from the soma and axon, as both EPSPs and dendritic spikes attenuate through the leaky dendritic cable (Figure 3E). Our model, however, did not account for the fact that distal branches on average contain more powerful synapses, which may boost the representation of these branches at the soma (Magee and Cook, 2000; Nicholson and Geinisman, 2009; Nicholson et al., 2006) and thus minimize the distance dependence of branch output. Combining the results of the present study with previous results (Magee and Cook, 2000; Nicholson and Geinisman, 2009; Nicholson et al., 2006), we propose that synapse strength increases along the somato-dendritic axis but decreases along the length of each radial oblique branch (Figure 3F). Additionally, the contribution of the dendritic spike from some branches could be enhanced by ion channel gradients that shift the initiation zone to more proximal portions of the branch or by broadening the dendritic spike.

Although asynchronous input may lead to global integration (Gasparini and Magee, 2006), our data suggest that synapses located more distally on a branch will contribute less to neuronal output during this integration mode. During more synchronous synaptic input, however, dendritic branches are likely to generate spikes (Gasparini and Magee, 2006). Our ssEM and modeling results show that synapses are scaled in the direction of normalizing the contribution of individual inputs to dendritic spikes, increasing the output of a branch when a group of synapses trigger a local dendritic spike and thus pointing to the importance of these spikes as fundamental units of synaptic integration in CA1 pyramidal neurons. The capacity to perform multi-layer computations enhances the computational power of individual neurons in a network (Polsky et al., 2004; Spruston and Kath, 2004), so it will be important to determine whether other types of neurons employ a similar integration scheme.

## EXPERIMENTAL PROCEDURES

### Institutional Approval

All experiments were performed using protocols approved by the Northwestern University Institutional Animal Care and Use Committee.

### Electron Microscopy

Adult rats (6 months old) were anesthetized with an injection of ketamine and xylazine. Biotinylated dextran amine (BDA-3000, Invitrogen; 10% dissolved in 0.12M phosphate buffered saline; PBS) was injected into the subiculum (from bregma: AP = -2.5, ML = +1.5; DV = -4.1) using either pressure injection (0.05  $\mu$ l/min for 5 min) or iontophoresis (5  $\mu$ A, alternating at 10 sec on/off for 6 min). After five days of recovery from surgery, rats were perfused with a fixative containing 3.5% paraformaldehyde, 0.1% glutaraldehyde, and 15% (v/v) picric acid in PBS. Brains were removed, hemisectioned, postfixed in fixative, rinsed in PBS, and then cut into 60  $\mu$ m-thick slices using a vibratome.

Individual slices were then rinsed in PBS, cryoprotected in ascending concentrations of sucrose and glycerol in PBS, freeze-thawed over liquid nitrogen 3 times, treated with 1% sodium borohydride in PBS, incubated in 0.3% hydrogen peroxide, and then rinsed. Slices were then rinsed in blocking solution (0.5% BSA, 1% nonfat dry milk, and 5% normal goat serum), and incubated in avidin-biotinylated horseradish peroxidase (HRP) using the



Vectastain ABC Elite Kit (Vector Laboratories, PK-6100 Standard, 1:300) for 36 hours at 4° C. Slices were then rinsed thoroughly and the BDA-HRP complex was visualized using diaminobenzidine as chromogen (Sigma, SK-4100) under gentle agitation for 10–120 min. Slices containing isolated individually labeled CA1 pyramidal neurons were then rinsed, treated with 0.67% osmium tetroxide and 1% uranyl acetate, dehydrated in graded ethanols, infiltrated with Araldite (Araldite 502), and cured in a drying oven at 60° C for 48 hours for conventional serial section electron microscopy.

Slices were trimmed to isolate the labeled dendrites of CA1 neurons, cut into 68 nm thin serial sections (100–500 serial sections) using an ultramicrotome (UCT, Leica), and mounted onto gold-gilded nickel slotted grids. Grids were counter-stained with 3% aqueous uranyl acetate and Reynold's lead citrate, and then mounted in an electron microscope (JEOL 100CX) to photograph serial sections containing dendritic segments within CA1 stratum radiatum in their entirety. Dendritic segments near branch ends were considered to be those segments that could be followed through >50 serial sections, and then disappear in subsequent serial sections. Branch-origin dendritic segments were readily identifiable due to their bifurcation from the primary apical dendrite. Second-order dendritic segments (i.e., those connecting a branch off the primary apical dendrite with a daughter terminal dendritic segment) were excluded from analyses.

Electron micrograph negatives were scanned using a PowerLook 2100XL scanner, organized into image stacks for each dendritic segment, and then analyzed and reconstructed using ImageJ (Rasband, 1997–2007) and Reconstruct (Fiala, 2005), respectively. Postsynaptic density (PSD) area and spine volume were measured using the same methods as previously described (Nusser et al., 1998; Racca et al., 2000; Nicholson et al., 2006; Nicholson & Geinisman, 2009). Briefly, for each spine and each synapse, all PSD or spine profiles on the electron micrographs of serial sections were measured in ImageJ. PSD area was estimated as the product of the summed PSD length and the section thickness (estimated to be 68 nm). When present, perforations or cytoplasmic areas of the spine head not containing a PSD profile were not included in the measurements. Spine volume was estimated as the product of the summed spine surface area values and section thickness.

### Post-embedding immunogold electron microscopy

AMPA-type receptor immunoreactivity was assessed as previously described (Nicholson et al., 2006). Synapses in CA1 stratum radiatum were included in the analysis only if their host spine could be followed to its spine neck ( $n = 342$ ). Because of the low-electron density of freeze-substituted tissue, it was impossible, except in fortuitous cases, to follow spines to their parent dendrite. Importantly, however, our measurements are within those reported previously for synapses in CA1 stratum radiatum (Harris et al., 1992; Nusser et al., 1998).

### Computational modeling

The CA1 pyramidal neuron morphology used in all simulations was reconstructed from a rat hippocampal pyramidal neuron described previously (Golding et al., 2001). All simulations were performed using the NEURON simulation environment (Hines and Carnevale, 1997).

The model included membrane capacitance and resistance as well as the active conductances sodium ( $\text{Na}$ ), delayed rectifier potassium ( $\text{K}_{\text{DR}}$ ), and A-type potassium ( $\text{K}_{\text{A}}$ ). Passive properties were constrained by electrophysiological recording of voltage attenuation from the soma to dendrite in the reconstructed neuron (Golding et al., 2001), and the active conductances  $\text{Na}$  and  $\text{K}_{\text{DR}}$  were uniformly distributed.  $\text{K}_{\text{A}}$  in the primary apical dendrite was distributed based on experimental data (Hoffman et al., 1997), and  $\text{K}_{\text{A}}$  in oblique dendrites was uniformly distributed using the value at the point of connection with the

primary apical dendrite. The model will be made available on the authors' website ([www.northwestern.edu/dendrite](http://www.northwestern.edu/dendrite)).

Fast excitatory synaptic conductances were modeled as a difference of exponentials with a rise time constant of 0.2 ms, decay time constant 5.0 ms, and reversal potential of 0 mV. Dendritic spikes were defined as a voltage exceeding a threshold of  $-35$  mV.

For the simulations in Figure 3 involving the two-stage integration model, synapses were randomly drawn from a distribution starting at 5 synapses/ $\mu\text{m}$  from the branch origin through the first third of each branch and then dropping to 3.3 synapses/ $\mu\text{m}$  until the branch end. Synaptic weights were determined as follows: We randomly drew from the probability distributions in Figure 2B to determine the PSD area as a function of the location of the synapse. For the two-stage integration model, if the selected synapse was on the proximal third of the branch we drew from the measured distribution for dendritic segments near branch origins, if it was on the distal third of the branch we drew from the measured distribution for dendritic segments near branch ends, and if it was on the middle third of the branch we drew from the measured distribution for dendritic segments near branch centers. Once we determined the PSD area, we chose the corresponding particle number from Figure 2F. The synaptic weight was the particle number times 0.025 nS, which led to values for unitary synaptic conductance between 0.07 and 0.99 nS. For the global integration model, synapses on each branch were distributed uniformly at a density chosen to match the number of synapses per branch in the two-stage integration model. Synaptic conductance increased approximately linearly from 0.21 to 0.33 nS along each branch, leading to a similar amount of somatic depolarization for inputs at all branch locations. Total synaptic conductance was kept the same in both models in order to facilitate direct comparison.

## Supplementary Material

Refer to Web version on PubMed Central for supplementary material.

## Acknowledgments

Supported by the National Institutes of Health (NS-46064 to WLK and NS, NS-35180 to NS, and AG-17139 to YG) and Northwestern University (Presidential Fellowship to YK). The authors thank Krutika Lakhoo, Annie Liu, and Elizabeth Piekarczyk for technical support with analysis of EM images and David Ferster, Indira Raman, and Aryeh Warmflash for critical readings of the manuscript. We thank Drs. Kristen Harris and John Fiala for developing and sharing the Reconstruct program.

## REFERENCES

- Amaral DG, Witter MP. The three-dimensional organization of the hippocampal formation: a review of anatomical data. *Neuroscience* 1989;31:571–591. [PubMed: 2687721]
- Brun VH, Leutgeb S, Wu HQ, Schwarcz R, Witter MP, Moser EI, Moser MB. Impaired spatial representation in CA1 after lesion of direct input from entorhinal cortex. *Neuron* 2008;57:290–302. [PubMed: 18215625]
- Brun VH, Otnass MK, Molden S, Steffenach HA, Witter MP, Moser MB, Moser EI. Place cells and place recognition maintained by direct entorhinal-hippocampal circuitry. *Science* 2002;296:2243–2246. [PubMed: 12077421]
- Fiala JC. Reconstruct: a free editor for serial section microscopy. *J Microsc* 2005;218:52–61. [PubMed: 15817063]
- Gasparini S, Magee JC. State-dependent dendritic computation in hippocampal CA1 pyramidal neurons. *J Neurosci* 2006;26:2088–2100. [PubMed: 16481442]
- Gasparini S, Migliore M, Magee JC. On the initiation and propagation of dendritic spikes in CA1 pyramidal neurons. *J Neurosci* 2004;24:11046–11056. [PubMed: 15590921]

- Golding NL, Mickus TJ, Katz Y, Kath WL, Spruston N. Factors mediating powerful voltage attenuation along CA1 pyramidal neuron dendrites. *J Physiol* 2005;568:69–82. [PubMed: 16002454]
- Golding NL, Kath WL, Spruston N. Dichotomy of action-potential backpropagation in CA1 pyramidal neuron dendrites. *J Neurophysiol* 2001;86:2998–3010. [PubMed: 11731556]
- Golding NL, Spruston N. Dendritic sodium spikes are variable triggers of axonal action potentials in hippocampal CA1 pyramidal neurons. *Neuron* 1998;21:1189–1200. [PubMed: 9856473]
- Harris KM, Jensen FE, Tsao B. Three-dimensional structure of dendritic spines and synapses in rat hippocampus (CA1) at postnatal day 15 and adult ages: implications for the maturation of synaptic physiology and long-term potentiation. *J Neurosci* 1992;12:2685–2705. [PubMed: 1613552]
- Harris KM, Stevens JK. Dendritic spines of CA 1 pyramidal cells in the rat hippocampus: serial electron microscopy with reference to their biophysical characteristics. *J Neurosci* 1989;9:2982–2997. [PubMed: 2769375]
- Harvey CD, Svoboda K. Locally dynamic synaptic learning rules in pyramidal neuron dendrites. *Nature* 2007;450:1195–1200. [PubMed: 18097401]
- Harvey CD, Yasuda R, Zhong H, Svoboda K. The spread of Ras activity triggered by activation of a single dendritic spine. *Science* 2008;321:136–140. [PubMed: 18556515]
- Häusser M. Synaptic function: dendritic democracy. *Curr Biol* 2001;11:R10–12. [PubMed: 11166188]
- Hines ML, Carnevale NT. The NEURON simulation environment. *Neural Comput* 1997;9:1179–1209. [PubMed: 9248061]
- Hoffman DA, Magee JC, Colbert CM, Johnston D. K<sup>+</sup> channel regulation of signal propagation in dendrites of hippocampal pyramidal neurons. *Nature* 1997;387:869–875. [PubMed: 9202119]
- Kharazia VN, Phend KD, Rustioni A, Weinberg RJ. EM colocalization of AMPA and NMDA receptor subunits at synapses in rat cerebral cortex. *Neurosci Lett* 1996;210:37–40. [PubMed: 8762186]
- Kharazia VN, Weinberg RJ. Immunogold localization of AMPA and NMDA receptors in somatic sensory cortex of albino rat. *J Comp Neurol* 1999;412:292–302. [PubMed: 10441757]
- Losonczy A, Magee JC. Integrative properties of radial oblique dendrites in hippocampal CA1 pyramidal neurons. *Neuron* 2006;50:291–307. [PubMed: 16630839]
- Losonczy A, Makara JK, Magee JC. Compartmentalized dendritic plasticity and input feature storage in neurons. *Nature* 2008;452:436–441. [PubMed: 18368112]
- Magee JC, Cook EP. Somatic EPSP amplitude is independent of synapse location in hippocampal pyramidal neurons. *Nat Neurosci* 2000;3:895–903. [PubMed: 10966620]
- Megias M, Emri Z, Freund TF, Gulyas AI. Total number and distribution of inhibitory and excitatory synapses on hippocampal CA1 pyramidal cells. *Neuroscience* 2001;102:527–540. [PubMed: 11226691]
- Nicholson DA, Geinisman Y. Axospinous synaptic subtype-specific differences in structure, size, ionotropic receptor expression, and connectivity in apical dendritic regions of rat hippocampal CA1 pyramidal neurons. *J Comp Neurol* 2009;512:399–418. [PubMed: 19006199]
- Nicholson DA, Trana R, Katz Y, Kath WL, Spruston N, Geinisman Y. Distance-dependent differences in synapse number and AMPA receptor expression in hippocampal CA1 pyramidal neurons. *Neuron* 2006;50:431–442. [PubMed: 16675397]
- Nusser Z, Lujan R, Laube G, Roberts JD, Molnar E, Somogyi P. Cell type and pathway dependence of synaptic AMPA receptor number and variability in the hippocampus. *Neuron* 1998;21:545–559. [PubMed: 9768841]
- Polsky A, Mel BW, Schiller J. Computational subunits in thin dendrites of pyramidal cells. *Nat Neurosci* 2004;7:621–627. [PubMed: 15156147]
- Rall W. Branching dendritic trees and motoneuron membrane resistivity. *Exp Neurol* 1959;1:491–527. [PubMed: 14435979]
- Rasband, WS. ImageJ. National Institutes of Health; Bethesda, Maryland, USA: 1997–2007. <http://rsb.info.nih.gov/ij/>
- Spruston N. Pyramidal neurons: dendritic structure and synaptic integration. *Nat Rev Neurosci* 2008;9:206–221. [PubMed: 18270515]
- Spruston N, Kath WL. Dendritic arithmetic. *Nat Neurosci* 2004;7:567–569. [PubMed: 15162161]



Tanaka J, Horiike Y, Matsuzaki M, Miyazaki T, Ellis-Davies GC, Kasai H. Protein synthesis and neurotrophin-dependent structural plasticity of single dendritic spines. *Science* 2008;319:1683–1687. [PubMed: 18309046]

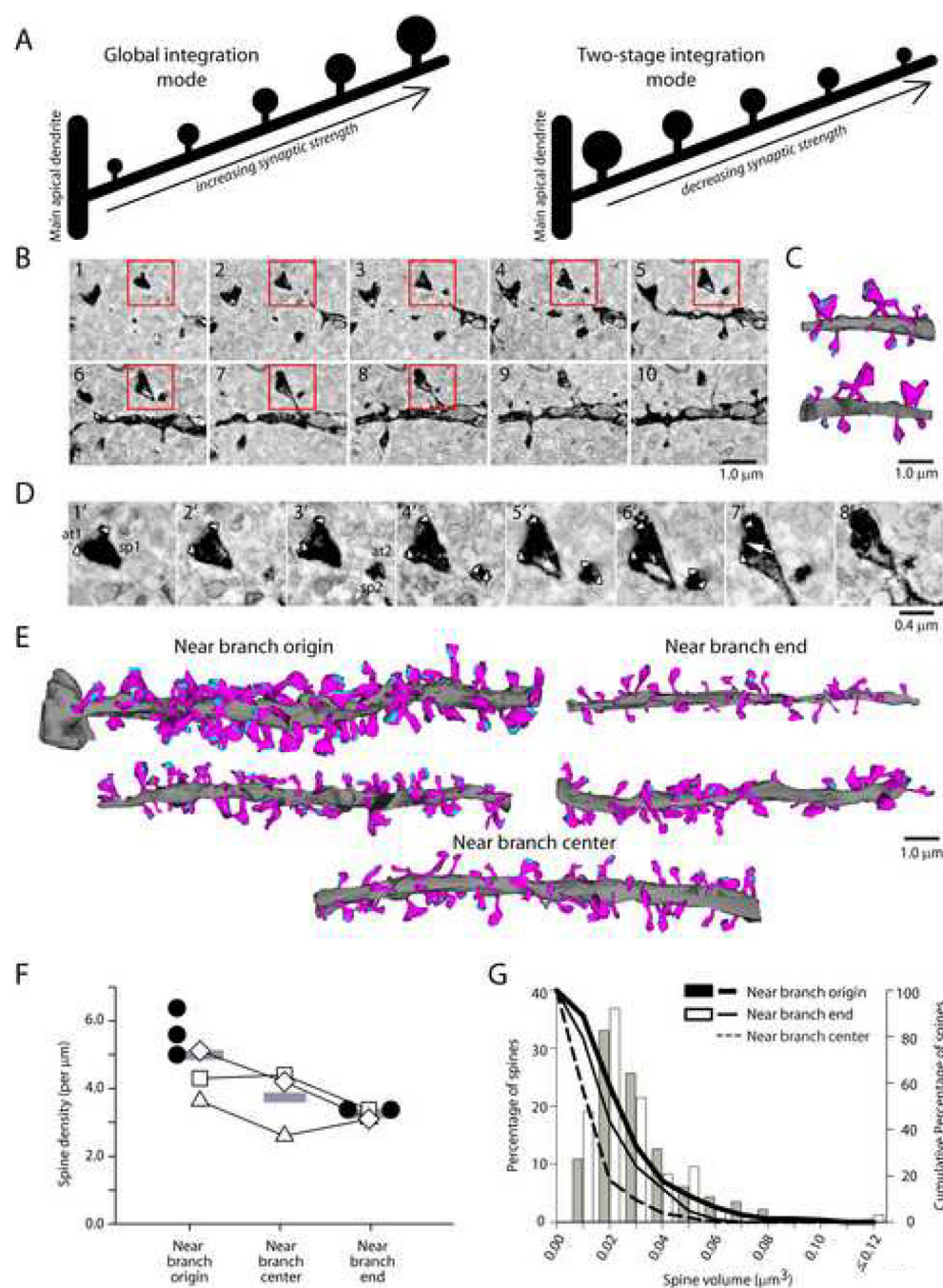


**Figure 1. Contrasting Models of Synaptic Integration / Spines Near and Far from the Primary Apical Dendrite**

(A) Schematic showing the predicted distribution of synaptic conductance along an individual apical oblique dendritic branch if synapses are scaled to normalize somatic EPSP amplitude (left) or the probability of initiating a dendritic spike (right).

(B) Serial-section electron microscopic view of a segment of dendrite with spines and synapses.

(C) Three-dimensional reconstruction of the segment shown in (B). Dendrite is shown in grey, spines are shown in purple, and postsynaptic densities (PSDs) are shown in blue. Top

panel is the reconstruction in its orientation as shown in the electron micrographs. Bottom panel is the reconstruction rotated 180°.

(D) Higher magnification serial electron micrographs of the boxed regions in (B). Electron micrographs show two dendritic spines (sp1 and sp2) making synapses with presynaptic axon terminals (at1 and at2). The borders of the PSDs are marked by white arrowheads and the full arrow indicates a perforation.

(E) Three-dimensional reconstructions of segments of the same dendrite (bottom three segments) and different dendrites (top two segments).

(F) Scatter plot showing spine densities in dendritic segments near branch origins, near branch ends, and near branch centers. Open symbols represent segments from the same branch, filled symbols represent segments from different branches, and lines show the means.

(G) Histogram showing the relative and cumulative frequencies of spine volumes in dendritic segments near branch origins, near branch ends, and near branch centers.

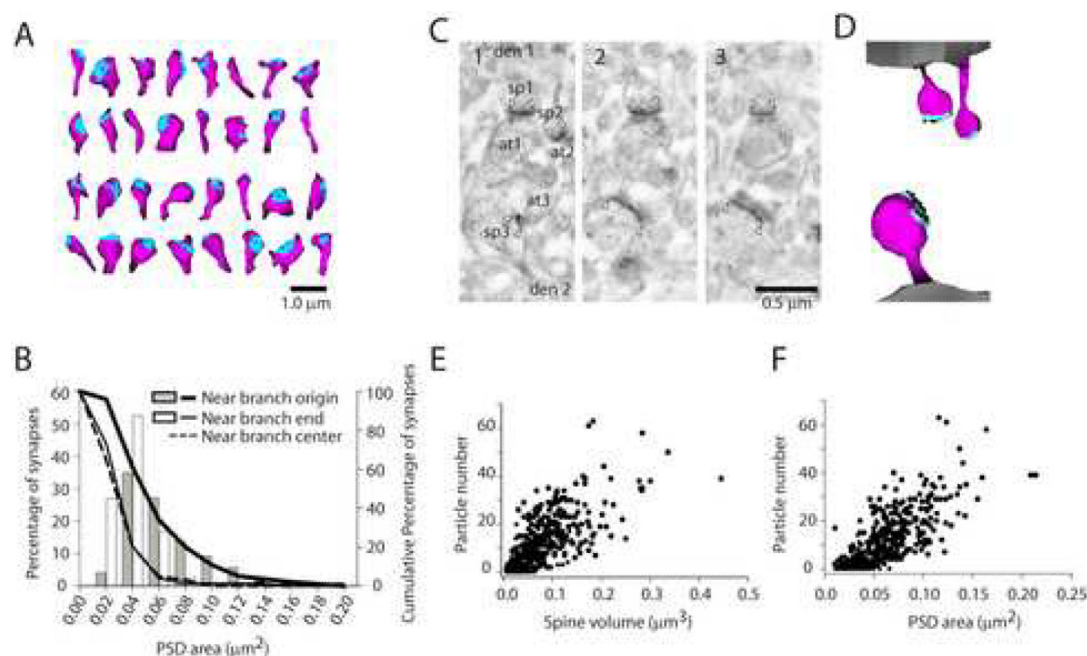


**Figure 2. Synapses near and far from the primary apical dendrite**

(A) Reconstructions of several spines and synapses.

(B) Histogram showing the relative and cumulative frequencies of PSD areas in dendritic segments near branch origins, near branch ends, and near branch centers.

(C) Electron micrographs of serial sections showing postembedding immunogold labeling of AMPA receptors.

(D) Three-dimensional reconstruction of synapses (blue), their spines (purple), and the synaptic immunogold particles (black) shown in C.

(E) Correlation of particle number with spine volume.

(F) Correlation of particle number with PSD area.

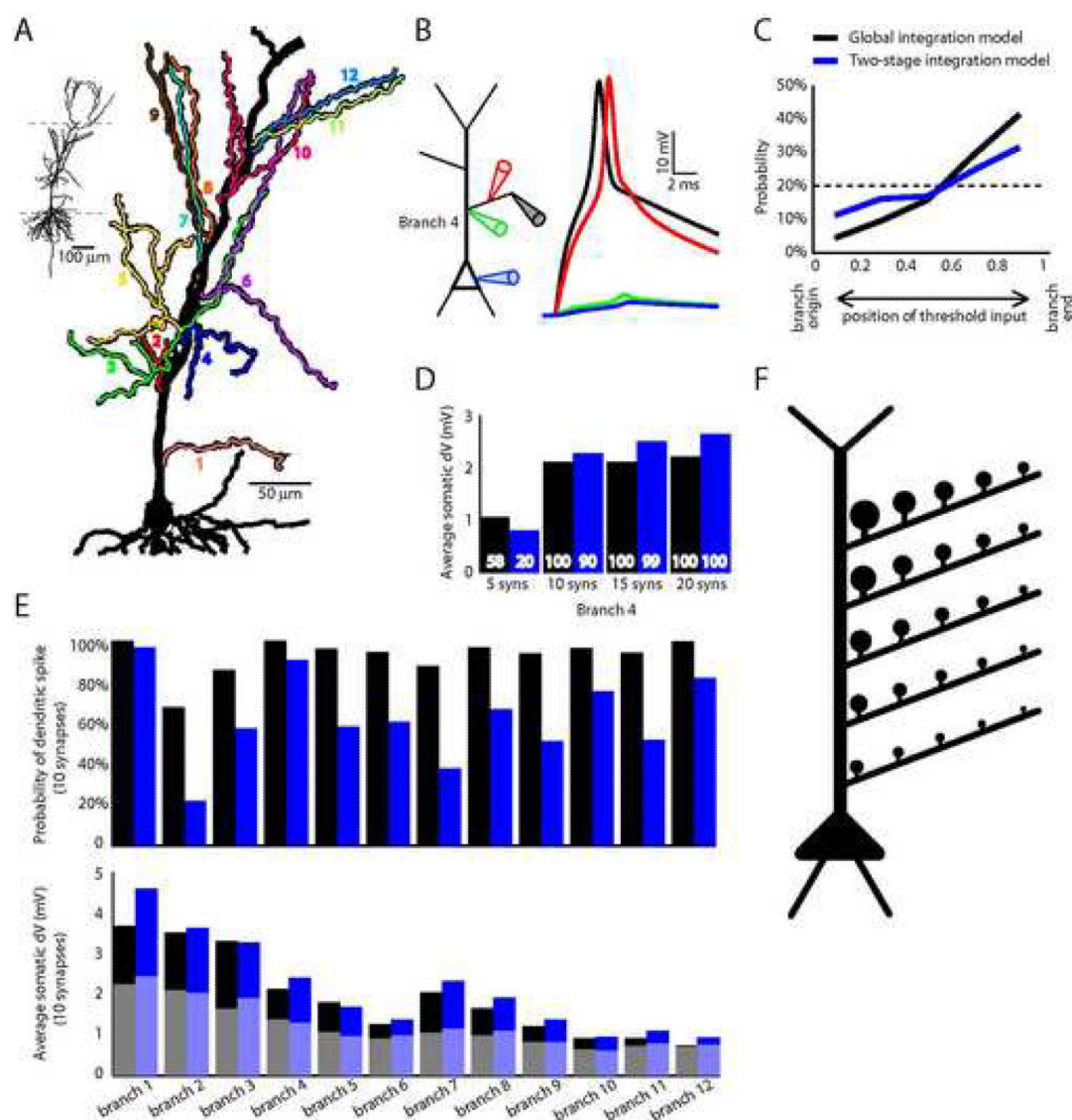


**Figure 3. Functional consequences of synapse distribution**

(A) The reconstructed CA1 pyramidal neuron morphology used for the models and the apical oblique dendrites used for the simulations (region between dashed lines enlarged).

(B) Sample voltage traces from a simulation in which fifteen synapses were randomly selected and activated on branch 4 in the two-stage integration model (188  $\mu\text{m}$  from the soma). Voltage is indicated at the branch end (black trace), center of the branch (red trace), branch origin (green trace), and soma (blue trace). Synapses were distributed along each branch shown in (A) with decreasing density and strength from branch origin to branch end as observed experimentally (two-stage integration model) and the reverse (global integration model).

(C) For each branch, synapses were randomly activated until a dendritic spike occurred (200 trials/branch). Probability distribution (bin size = 0.2) showing the location along the dendritic branch of the input triggering the spike (the last synapse selected) for the two models (black and blue lines). The dashed line indicates the uniform distribution expected if the final input contributes equally to the spike at all locations.

(D) Somatic depolarization averaged over 500 trials resulting from activation of 5, 10, 15, and 20 synapses in the two models: global integration (black bars) and two-stage integration (blue bars).



(blue bars). The white numbers indicate the percentage of trials that resulted in a dendritic spike.

(E) Top: The percentage of trials resulting in a dendritic spike for the global (black bars) and two-stage (blue bars) integration models when ten synapses are activated on each branch (500 trials per branch). Bottom: The average somatic depolarization resulting from these simulations shown separately for trials in which a dendritic spike was triggered (dark bars) and trials that did not produce a dendritic spike (light bars).

(F) Schematic of the proposed synapse distribution for the CA1 apical dendritic tree based upon previous (Nicholson et al., 2006, Magee and Cook, 2000) and current results.